ROYAL SOCIETY
OF CHEMISTRY

PAPER

Check for updates

Multi-interface synergistic photocatalytic 2D/0D/2D TiO2/Pd/Ti3C2 heterojunctions for boosting hydrogen production

Huimin Jia, [ID] [a] Ya Wang,[a] Yiting Yang,[ab] Chuang Liu[a] and Weiwei He [ID] *[a]

Constructing a multi-interface synergistic catalytic system represents an effective strategy for developing highly efficient photocatalysts; however, the challenge lies in fabricating ideal heterojunctions that can fully harness the multiple synergistic effects of the components. In this study, a series of TiO2/Pd/Ti3C2 nanocomposite photocatalysts with 2D/0D/2D heterojunctions were successfully fabricated through a combination of photoreduction and electrostatic self-assembly techniques by varying the mass ratios. Under irradiation from a 300 W xenon lamp, the as-constructed TiO2/3% Pd/1% Ti3C2 heterojunction photocatalyst exhibited a significantly enhanced H2 evolution rate of 21.60 mmol h^{-1} g^{-1}, which was approximately 135-fold and 25.4-fold higher than those of pristine TiO2 nanosheets (NSs) and TiO2/1% Ti3C2, respectively. Electrochemical impedance spectroscopy, photoluminescence spectroscopy, and electron spin resonance analysis collectively revealed that the enhanced photocatalytic performance can be attributed to the formation of a synergistic catalytic interface among the TiO2 NSs, highly active Pd NPs, and monolayer Ti3C2 nanosheets. This interface facilitated efficient charge separation, shortened the charge transfer pathways, and enhanced the generation of reactive oxygen species. This study presents a promising strategy for improving catalytic performance through multi-interface synergy and offers a preliminary investigation into the underlying synergistic mechanisms using multiple characterization techniques.

Introduction

To reach carbon neutrality and tackle global energy issues, it is essential to pursue clean, sustainable energy sources. Hydrogen is one of the most important clean energy sources with a high energy density and is considered a renewable, carbon–neutral energy source.[1,2] Photocatalytic water splitting is a promising strategy to generate clean and renewable hydrogen.[3] TiO2 is considered a promising semiconductor and is extensively studied because of its outstanding stability, richness and nontoxic nature.[4,5] However, the inefficient light absorption induced by its band gap and the issues of easy recombination and slow transport dynamics of the photo-generated carriers severely restrict its applications.[6,7] To address these issues, extensive scientific efforts have been put forward, leveraging strategies such as co-catalyst loading, elemental doping, surface modification, and heterojunction construction.[8–10] Specifically, both co-catalyst modification strategies and heterojunction

engineering—offering efficient interfacial charge transport—have been widely recognized as remarkable approaches to inhibit the recombination rate and extend the lifespan of photogenerated charge carriers.[11,12] On this basis, the deposition of a co-catalyst on TiO2 is an effective method to accelerate the photogenerated charge carrier transport, acquire high visible-light absorption capacity and improve the photocatalytic H2 production performance. As a co-catalyst, similar to Pt, Pd has a large work function that offers it an outstanding capability to trap electrons, which in turn achieves efficient charge separation/transfer.[13,14] Furthermore, Pd has a price that is far lower than those of Au and Pt; hence, it is deemed an ideal cocatalyst for photocatalytic H2 evolution.

Ti3C2 MXene, an emerging two-dimensional (2D) transition metal carbide, has gained much interest in the fields of energy conversion and storage, biosensing, electromagnetic interference shielding, and catalysis.[15,16] Its fascinating intrinsic characteristics, such as light-harvesting ability, excellent metallic conductivity, large specific surface area, and low Fermi level, indicate that Ti3C2 MXene has remarkable potential as an effective co-catalyst to decorate photocatalytic materials for reducing the light scattering and promoting the separation and transfer of photogenerated charge carriers.[17,18] For photocatalytic H2 production, Ti3C2 with exposed surface-active metal sites has been shown to be a useful co-catalyst.[19,20] However, the

[a]Key Laboratory of Micro-Nano Materials for Energy Storage and Conversion of Henan Province, Institute of Surface Micro and Nano Materials, College of Chemical and Materials Engineering, Xuchang University, Xuchang, Henan, 461000, P. R. China. E-mail: heweiweixcu@gmail.com

[b]School of Nanoscience and Materials Engineering, Henan University, Kaifeng, Henan, 475004, P. R. China

co-catalytic H_2 evolution activity of Ti_3C_2 MXene is still unsatisfactory. A series of heterojunction materials based on Ti_3C_2 was created, and an obvious enhancement in H_2 production was reported.[21–23] Therefore, it is meaningful to combine semiconductor materials with precious metals with electron enrichment, as well as single-layer Ti_3C_2 materials with large specific surface areas and excellent conductivity and photothermal properties, to further reduce the photogenerated carrier recombination efficiency and construct efficient semiconductor catalysts.

Based on the above-mentioned considerations, we constructed a TiO_2 nanosheet (NS), Pd NP and monolayer Ti_3C_2 NS co-catalyst synergistic $TiO_2/Pd/Ti_3C_2$ nanocomposite with 2D/0D/2D heterojunctions for improved photocatalytic hydrogen production via photoreduction and electrostatic self-assembly. The photocatalytic H_2 production activity of the $TiO_2/Pd/Ti_3C_2$ nanocomposite catalysts with different mass ratios was studied, and cyclic experiments were conducted to establish the stability of the composite materials. The surface composition, microstructure, light-harvesting ability, chemical state of elements and charge, separation/transport of the TiO_2/Pd co-catalyst and $TiO_2/Pd/Ti_3C_2$ heterojunctions were systematically investigated. Furthermore, electron spin resonance (ESR) techniques were employed to analyze the interaction mechanism of the $TiO_2/Pd/Ti_3C_2$ nanocomposites to improve the photocatalytic H_2 evolution activity. The experimental analyses clarified that the $TiO_2/$ 3% Pd/1% Ti_3C_2 heterojunction nanocomposites showed rapid transport of photogenerated charges, exceptional light absorption, and enhanced photocatalytic H_2 evolution, which benefited from the shorter charge transport distance and the effective separation of photogenerated charges at the interface of the $TiO_2/3\%$ Pd/1% Ti_3C_2 2D/0D/2D heterojunctions. This study provides design ideas for catalysts that can improve the performance of TiO_2 photocatalytic decomposition of aqueous hydrogen by interfacial contact and multi-interface synergism.

2. Experimental

2.1. Materials

Tetra-n-butyl titanate (TNBT), hydrogen tetrachloroplatinate (H_2PdCl_4), hydrofluoric acid (HF), and 3,3′,5,5′-tetramethylbenzidine (TMB) were obtained from Sinopharm Chemical Reagent Co., Ltd (Shanghai, China). Ascorbic acid (AA) was purchased from Aladdin Biochemical Technology Co., Ltd. Sodium azide (NaN_3), triethanolamine (TEOA), isopropanol (IPA), superoxide dismutase (SOD) and tetramethylammonium hydroxide (TMAH) were obtained from Sigma-Aldrich (MO, USA). Sodium borohydride ($NaBH_4$) was purchased from Tianjin Kemiou Chemical Reagent Co., Ltd. The spin traps, 5,5-dimethyl-1-pyrroline-N-oxide (DMPO) and 2,2,6,6-tetramethyl-4-piperidone (TEMP) were purchased from Dojindo China CO., Ltd (Shanghai, China). All the reagents mentioned above were of analytical reagent grade and were utilized without additional purification. Milli-Q water (18 MΩ cm) was employed to prepare all solutions.

2.2. Preparation of the TiO_2 (nanosheets) NSs and $TiO_2@Pd$ composites

According to the previous report, TiO_2 NSs were prepared via a hydrothermal method. Typically, 5 mL tetra-n-butyl titanate (TNBT) and 1 mL hydrofluoric acid (HF) were mixed and stirred for 10 min. Next, the mixture was moved into a stainless-steel autoclave lined with Teflon and placed in an oven set at 200 °C for 24 hours. The resulting precipitate was purified and rinsed three times, using 0.1 mol L^{-1} NaOH solution, ethanol, and deionized water in sequence. Finally, the product was dried overnight in a vacuum oven at 60 °C.

To prepare the Pd nanoparticle-modified TiO_2 NSs, a simple photoreduction approach was employed. In a typical procedure, 50 mg of TiO_2 NSs was dispersed in 10 mL of deionized water and ultrasonically dispersed for 30 min, then 1 and 3 wt% of 30.08 mM H_2PdCl_4 solution was added. The mixture was stirred for 30 min under 300 W xenon lamp irradiation with a wavelength range of 320 to 780 nm. Lastly, the Pd-modified TiO_2 NSs were obtained by centrifugation and washing several times with deionized water, then vacuum-dried overnight at 60 °C. The obtained samples were named $TiO_2@1\%$ Pd and $TiO_2@3\%$ Pd.
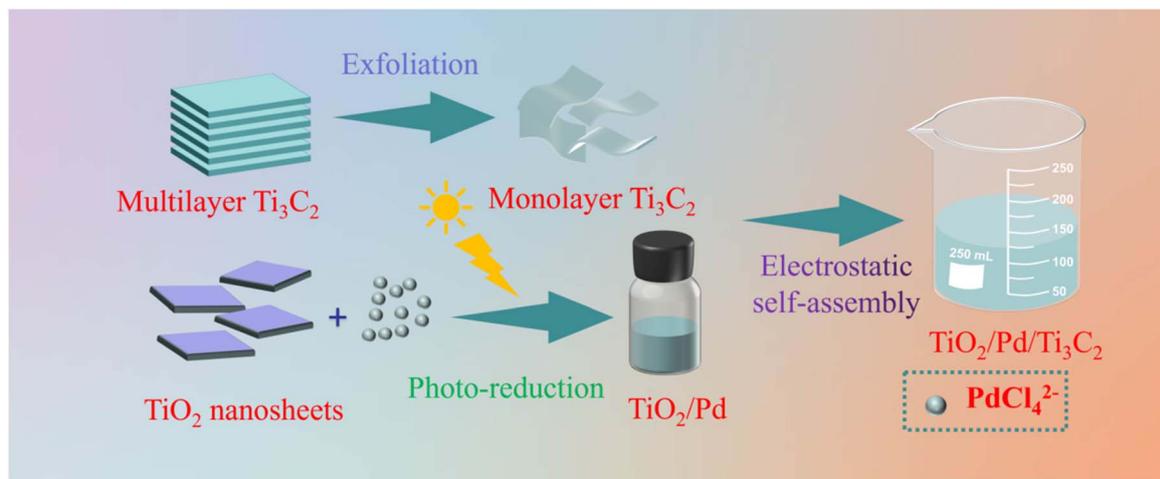
2.3. Preparation of monolayer Ti_3C_2 NSs

According to the previous report, Ti_3C_2 MXene nanosheets (NSs) were synthesized through an HF etching treatment using a Ti_3AlC_3 precursor.[24,25] For a typical preparation process, 1.0 g Ti_3AlC_2 was dispersed in 10 mL of 50 wt% hydrofluoric acid, and this mixture was moved to a continuously stirred tank reactor with a Teflon lining. The etching was performed over 24 hours with non-stop stirring. The sample was then centrifuged at 3500 rpm for 10 minutes, then washed with DI water, and dried overnight in an oven set at 80 °C under an air atmosphere. The resulting product is named titanium carbide, also known as Ti_3C_2 MXene.

2.4. Preparation of $TiO_2/Pd/Ti_3C_2$ nanocomposites

The preparation strategy of $TiO_2/Pd/Ti_3C_2$ nanocomposites is illustrated in Scheme 1. The prepared TiO_2/Pd (50 mg) was dispersed in a beaker containing 50 mL of deionized water. Then, single-layer Ti_3C_2 solutions (0.55 mg mL^{-1}) with mass ratios of 1% and 3% to TiO_2 were added, respectively. The beaker was then placed in an ultrasonic cleaner and ultrasonically dispersed for 30 minutes, with the water temperature maintained below 30° to prevent Ti_3C_2 from oxidizing due to high temperature. The well-dispersed mixed solution was left to stand for 30 minutes until the precipitate settled at the bottom of the beaker. The supernatant was removed, and the remaining precipitate solution was centrifuged and washed once, then placed in a vacuum drying oven and dried at 60 °C for 12 h. The dried samples were respectively marked as $TiO_2/1\%$ Pd/1% Ti_3C_2, $TiO_2/1\%$ Pd/3% Ti_3C_2 and $TiO_2/3\%$ Pd/1% Ti_3C_2 for future use. For comparison, $TiO_2/1\%$ Ti_3C_2 and $TiO_2/3\%$ Ti_3C_2 composite nanomaterials were prepared by the same method.

Scheme 1 Preparation process of the monolayer Ti_3C_2 MXene and TiO_2/Pd and $TiO_2/Pd/Ti_3C_2$ nanocomposites.

2.5. Characterizations

X-ray diffraction (XRD, Bruker D8 Advance diffractometer) with monochromatic Cu Kα radiation (1.5418 Å) was used to identify the phase composition. Transmission electron microscopy (TEM) images were acquired using a Tecnai G2 F20 U-Twin electron microscope (FEI, USA) with an accelerating voltage of 200 kV, and this same instrument was also employed for HRTEM analysis. X-ray photoelectron spectroscopy (XPS) was conducted on an ESCALAB 250Xi spectrometer (Thermo Fisher Scientific, USA), utilizing 150 W Al Kα radiation and a base pressure of $\sim 3 \times 10^{-9}$ mbar. All binding energies were calibrated against the C 1s peak at 284.8 eV. Electron paramagnetic resonance (EPR) spectra were used to detect ROS by electron spin paramagnetic spectroscopy (Bruker EMX micro). Ultraviolet-visible absorption spectra and diffuse reflectance spectra (DRS) were obtained with a UV-Vis-NIR Spectrometer (Varian Cary 5000). Photoluminescence spectroscopy (PL) was conducted with a Hitachi F4600 instrument, while transient fluorescence spectra were measured with a LifeSpec II Lifetime Spectrometer. All Photoelectrochemical (PEC) experiments were performed using an electrochemical workstation (CHI660E, Chen Hua Instruments Co., Ltd, Shanghai, China) under light irradiation. The photoelectrodes were made from the fabricated sample, a platinum wire, and Ag/AgCl (with saturated KCl), serving as the working electrode, counter electrode, and reference electrode, respectively. The electrochemical impedance spectroscopy (EIS) measurements were obtained in 0.1 M KCl solution containing $Fe(CN)_6^{3-/4-}$ (1 mM) with a frequency range from 0.01 Hz to 10 000 kHz.

2.6. Electron spin resonance (ESR) spectroscopy measurements

ESR spectra were recorded on a Bruker EMX system with a 300 W xenon lamp at room temperature. A mixed solution of 50 μL (5 μL of 1 mg mL^{-1} catalyst, 5 μL of scavenger, and 40 μL of water) was placed in a quartz capillary with an inner diameter of 0.9 mm and sealed at the bottom with wax. The capillary was

inserted into the ESR test chamber, and the spectra were collected after irradiation for a certain period of time. 250 mM BMPO was used to capture $O_2^{\cdot-}$ (in water as the solvent), 50 mM DMPO was used to capture ·OH, 100 mM TEMP was used to capture $^1O_2$, and 100 mM TEMPO was used to capture photogenerated electrons. The test parameters were 20 dB microwave attenuation, 2 mW microwave power for detecting spin adducts, a scan range of 100 G, and a field modulation of 1 G.

2.7. Photocatalytic hydrogen production

Photocatalytic hydrogen generation tests were performed in a closed system with a quartz reactor for evacuation and gas circulation. Solar light was simulated with a 300 W Xe lamp (Perfect, China). Typically, 15 mg of the sample was dispersed in a 100 mL mixture of water and methanol (v/v 9 : 1) while being stirred magnetically. Prior to light exposure, the reactor (fitted with a water-cooling jacket maintained at 25 °C) underwent 30 minutes of evacuation, and circulating condensate was supplied to it continuously. An online gas chromatograph, equipped with a TDX-01 column and a thermal conductivity detector (TCD), with argon as the carrier gas, was employed to analyze the generated hydrogen.

3. Results and discussion

3.1. Structural and morphology analyses

X-ray diffraction (XRD) characterization was conducted to analyze the crystal structures and phase purity of the prepared materials (TiO_2, Ti_3C_2, TiO_2/Pd, TiO_2/Ti_3C_2 and $TiO_2/Pd/Ti_3C_2$ composites), as illustrated in Fig. 1a. After etching treatment, the single-layer Ti_3C_2 exhibited the most prominent characteristic diffraction peak at an angle of 2θ of 6.2°, corresponding to the (002) crystal plane. The other diffraction peaks at 18.2° and 30.5° can be assigned to (004) and (006) crystal facets of the monolayer Ti_3C_2 (JCPDS 52-875). As shown in Fig. 1a, the diffraction peaks at 2θ values of 23.4, 37.7 and 47.9°, which are attributed to anatase TiO_2, correspond to the (101), (004) and
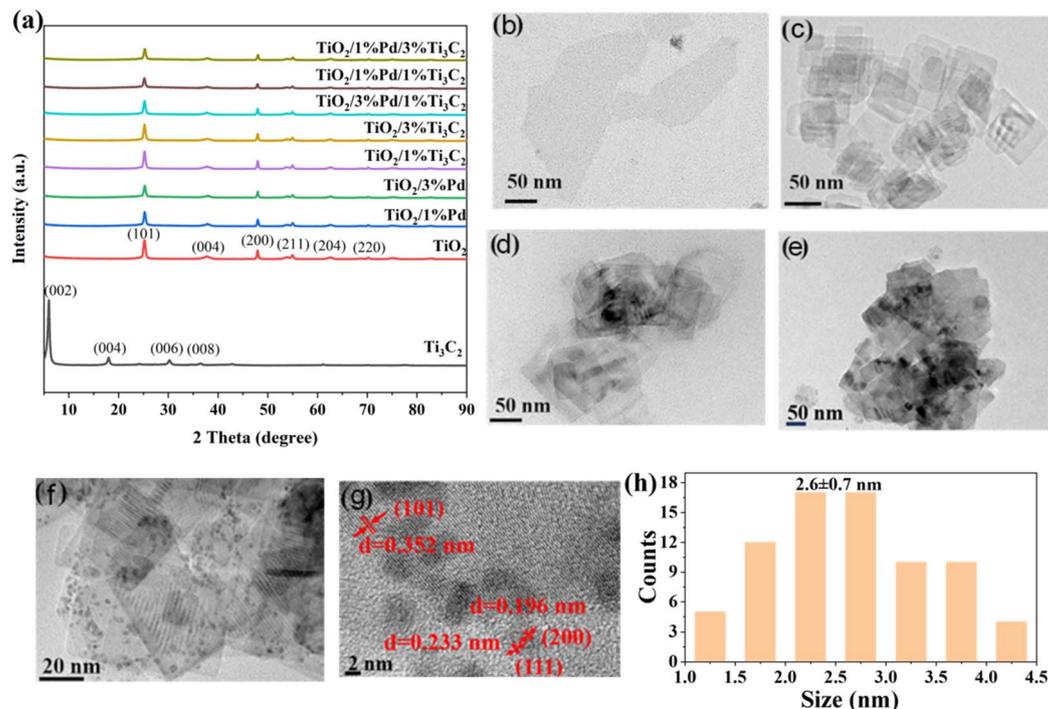
Fig. 1 (a) XRD patterns of TiO_2, TiO_2/Ti_3C_2, TiO_2/Pd and all-synthesized $TiO_2/Pd/Ti_3C_2$ composites. TEM images of (b) monolayer Ti_3C_2 MXenes, (c) TiO_2 nanosheets, (d) $TiO_2/1\%$ Ti_3C_2, (e) $TiO_2/3\%$ Pd, and (f) $TiO_2/3\%$ Pd/1% Ti_3C_2. (g) HRTEM image of $TiO_2/3\%$ Pd/1% Ti_3C_2. (h) Pd particle size distribution in $TiO_2/3\%$ Pd/1% Ti_3C_2.

(200) planes, respectively (PDF card 21-1272, JCPDS). However, no Pd NPs or monolayer Ti_3C_2 characteristic peaks were observed in the XRD diffraction patterns of TiO_2/Pd, TiO_2/Ti_3C_2, or $TiO_2/Pd/Ti_3C_2$ composite nanomaterials. This is because the amounts of loaded Pd NPs and Ti_3C_2 were relatively small, and no obvious characteristic peaks were displayed. Additionally, compared to the peaks of pure TiO_2, the positions of the diffraction peaks of the composite nanomaterials did not undergo significant changes, indicating that the crystal structure of TiO_2 was not affected during the preparation of the $TiO_2/Pd/Ti_3C_2$ nanocomposite material.

The morphology and compositional features of the obtained samples were investigated using TEM, HRTEM, and AFM techniques. Fig. 1b shows the TEM image of the exfoliated single-layer Ti_3C_2. It can be seen that the obtained monosingle-layer Ti_3C_2 has a two-dimensional sheet-like structure, approximately 200 nm in size, and with an irregular shape. Additionally, the thickness of Ti_3C_2 was measured using AFM, and it was found that the thickness of the single-layer Ti_3C_2 was 4.596 nm (Fig. S1). In Fig. 1c, TiO_2, as the substrate material, also presents a two-dimensional square sheet-like structure, but its thickness is greater than that of Ti_3C_2. Fig. 1d shows the TEM image of $TiO_2/1\%$ Ti_3C_2. Compared with pure TiO_2, it can be observed that there are samples mixed together, but it is impossible to confirm whether Ti_3C_2 is present. This might be related to the small amount of added Ti_3C_2 and the brightness contrast of the image. As shown in Fig. 1e, there are granular nanoparticles loaded on the TiO_2 NSs, which are presumed to be Pd. The corresponding TEM and HRTEM images of the $TiO_2/3\%$ Pd/1%

Ti_3C_2 nanocomposite, shown in Fig. 1f, illustrate that Pd nanoparticles are uniformly loaded on the TiO_2 NSs. In Fig. 1g, the clear lattice fringes of 0.352 nm, 0.223 nm and 0.196 nm were assigned to the (101) plane of TiO_2 and the (111) and (200) planes of Pd, respectively, indicating that Pd has been successfully loaded onto the TiO_2 NSs. Fig. 1h shows the histogram of the particle size distribution of Pd particles on the surface of the substrate material. It can be calculated that the average particle size of the loaded Pd particles is within the range of 2.6 ± 0.7 nm. To further investigate whether a successful composite with Ti_3C_2 was achieved, additional characterizations were conducted.

X-ray photoelectron spectroscopy (XPS) analysis was employed to determine the composition and binding environment of the samples of TiO_2, $TiO_2/3\%$ Ti_3C_2 and $TiO_2/3\%$ Pd/1% Ti_3C_2. The full-scale XPS spectrum of $TiO_2/3\%$ Pd/1% Ti_3C_2, presented in Fig. S2a, demonstrated that this nanocomposite was composed of Ti, C, O and Pt. Fig. 2a shows the higher resolution Ti 2p XPS spectra of TiO_2, $TiO_2/3\%$ Ti_3C_2 and $TiO_2/3\%$ Pd/1% Ti_3C_2, which show two peaks at approximately 458.7 and 464.4 eV, corresponding to Ti–O $2p_{3/2}$ and Ti–O $2p_{1/2}$, respectively.[26] It can also be seen from Fig. 3a that, in the $TiO_2/3\%$ Ti_3C_2 spectrum, a characteristic peak appears at 455.1 eV, which corresponds to Ti–C $2p_{3/2}$;[27] an enlarged image of the peak is displayed in Fig. S2b. The O 1s spectrum shows peaks at 529.7 eV, corresponding to Ti–O–Ti bonds in the TiO_2, $TiO_2/3\%$ Ti_3C_2 and $TiO_2/3\%$ Pd/1% Ti_3C_2, and the peak at 531.5 eV can be attributed to surface hydroxyl groups (–OH) and intermediate products of Pd during the reduction process (Fig. 2b). Surface –
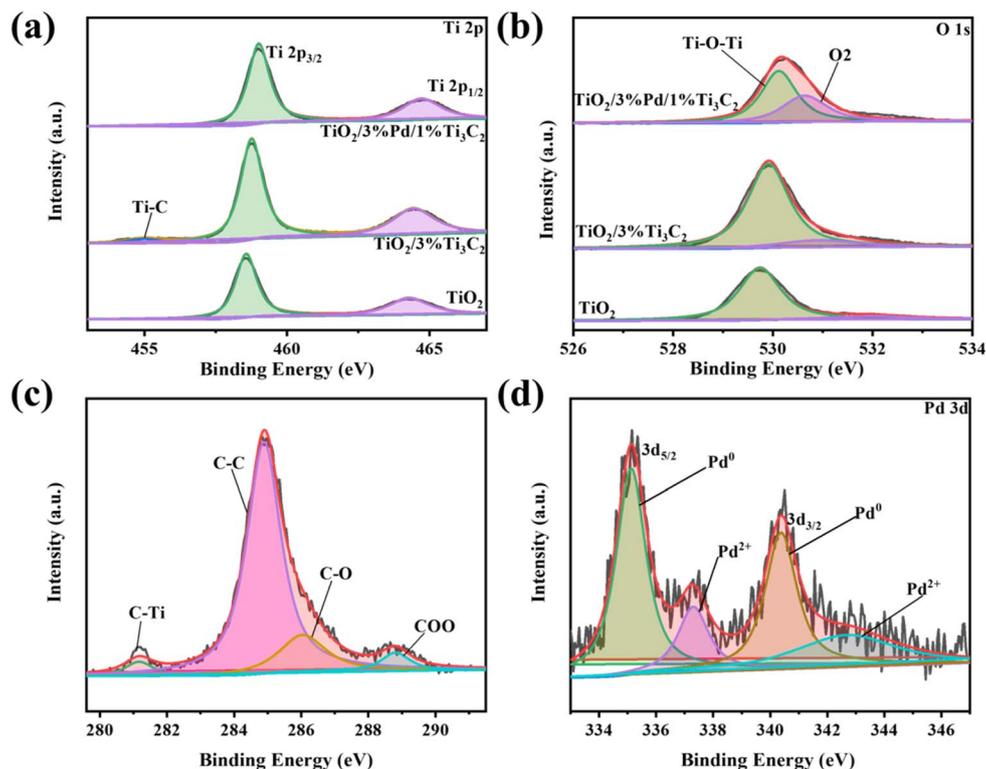
Fig. 2   High-resolution XPS spectra of (a) Ti 2p and (b) O 1s for TiO$_2$, TiO$_2$/3% Ti$_3$C$_2$ and TiO$_2$/3% Pd/1% Ti$_3$C$_2$. XPS spectra of (c) C 1s and (d) Pd 3d for TiO$_2$/3% Ti$_3$C$_2$ and TiO$_2$/3% Pd/1% Ti$_3$C$_2$, respectively.

OH can help the material disperse uniformly in water.[28] It is worth noting that the positions of the peaks of Ti 2p and O 1s in TiO$_2$/3% Ti$_3$C$_2$ and TiO$_2$/3% Pd/1% Ti$_3$C$_2$ both shift significantly in the direction of high binding energy as compared to that of the original TiO$_2$, indicating that electron transfer occurs at the interface after the composite with Ti$_3$C$_2$ and the loading of Pd NPs. As illustrated in Fig. 2c, the C 1s spectrum of TiO$_2$/3% Ti$_3$C$_2$ was deconvoluted into four distinct peaks, which can be ascribed to C–Ti (281.2 eV), C–C (284.8 eV), C–O (286.1 eV), and –O–C=O (288.1 eV), respectively.[29] The appearance of C–Ti bonds is due to Ti$_3$C$_2$, further verifying the successful formation of the composite of Ti$_3$C$_2$ and TiO$_2$. Fig. 2d shows the Pd 3d spectrum of the TiO$_2$/3% Pd/1% Ti$_3$C$_2$ composite material. Two significant peaks at 335.7 eV and 340.6 eV could be allocated to the Pd 3d$_{5/2}$ and Pd 3d$_{3/2}$ of Pd^0, respectively.[30] The peaks at 337.3 eV, 342.8 eV and 335.4 eV correspond to the Pd 3d of Pd^{2+}, indicating that the incorporated Pt atoms are in a partially oxidized state.

3.2.   Optical characterization

To determine the optical properties, the UV-Vis absorbance spectra were recorded as shown in Fig. 3a. The spectra clearly indicated that the absorption edge position of pure TiO$_2$ NSs is around 384 nm, corresponding to a band gap energy of 3.23 eV (Fig. S3a). However, the TiO$_2$/Pd/Ti$_3$C$_2$ nanocomposite materials, tailored for visible-light absorption, exhibit a marked increase in light absorption at longer wavelengths compared to pristine TiO$_2$, TiO$_2$/Pd and TiO$_2$/Ti$_3$C$_2$. This suggests that the

TiO$_2$/Pd/Ti$_3$C$_2$ nanocomposite materials modify the optical properties, allowing for enhanced absorption in the visible region. The PL spectrum was used to characterize the recombination of photogenerated electrons and holes in the as-prepared 2D/0D/2D TiO$_2$/Pd/Ti$_3$C$_2$ heterojunction nanocomposites. Steady-state photoluminescence (PL) spectroscopy is used to characterize the separation efficiency of photogenerated electron–hole (e–h$^+$) pairs. The relationship between carrier separation efficiency and signal peak intensity shows that a lower peak intensity corresponds to a higher efficiency.[31] In Fig. 3b, the pristine TiO$_2$ NSs show the strongest characteristic peak, which suggests the lowest efficiency of charge separation.[32] With the loading of Pd NPs and the combination with Ti$_3$C$_2$, the intensity of the PL spectrum gradually decreases. The characteristic peaks observed for TiO$_2$/3% Pd/1% are weaker than those detected for the other composite nanomaterial samples, indicating that the modified composite material improves the efficiency of the separation of photogenerated electron–hole pairs and hinders their recombination. This further proves the successful preparation of the composite materials.

Electrochemical impedance spectroscopy (EIS) was utilized to investigate the resistance associated with interfacial charge transfer. It is widely recognized that the semicircular diameter observed in a Nyquist plot is associated with charge-transfer resistance (R_{et}), which serves as an indicator of the charge transfer efficiency at the boundary between the electrode and the electrolyte. A smaller semicircular arc in the Nyquist plot
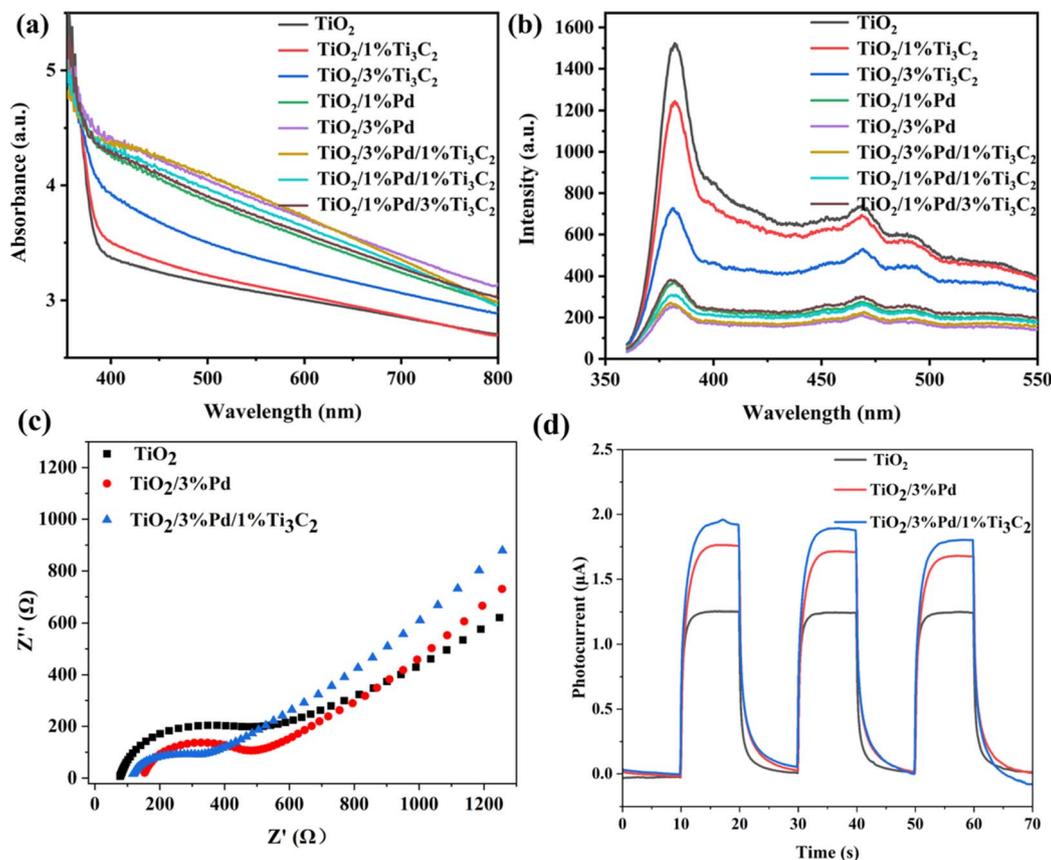
Fig. 3 (a) UV-vis absorption spectra and (b) photoluminescence (PL) spectra of TiO_2, TiO_2/Ti_3C_2, TiO_2/Pd and $TiO_2/Pd/Ti_3C_2$. (c) EIS spectra and (d) transient photocurrent of TiO_2, $TiO_2/3\%$ Pd and $TiO_2/3\%$ Pd/1% Ti_3C_2.

indicates lower interfacial resistance and improved charge transfer capability.[33] As shown in Fig. 3c, the 2D/0D/2D $TiO_2/Pd/Ti_3C_2$ heterojunction nanocomposites exhibit a notably smaller arc radius compared to those of TiO_2 and $TiO_2/3\%$ Pd, implying a reduction in charge transfer resistance. This observation indicates a more rapid separation rate of charge carriers, ultimately enhancing the electrical conductivity of the ternary composite system. The $TiO_2/3\%$ Pd/1% Ti_3C_2 heterojunction nanocomposite, with its suppressed charge recombination and improved charge separation efficiency, is expected to demonstrate superior photocatalytic activity under visible light. These EIS findings are consistent with the results obtained from the photoluminescence (PL) analysis. Furthermore, the transient PEC responses of TiO_2, $TiO_2/3\%$ Pd and $TiO_2/3\%$ Pd/1% Ti_3C_2 nanocomposite were recorded under light irradiation for 3 periodic on–off cycles. As displayed in Fig. 3d, the $TiO_2/3\%$ Pd/1% Ti_3C_2 exhibited a remarkably high anode photocurrent response of about 1.98 μA, which is about 1.8 and 1.2 times higher than those of TiO_2 and $TiO_2/3\%$ Pd, respectively, indicating that the photogenerated charge carrier lifetime in the $TiO_2/3\%$ Pd/1% Ti_3C_2 heterojunction nanocomposite is enhanced compared to those of the individual components.

3.3. Photocatalytic H_2-Evolution performance

Fig. 4 compares the photocatalytic hydrogen evolution over different composite nanomaterials. The control experiments

proved that no H_2 was produced when there was no catalyst or no light irradiation. The amount of H_2 produced increased dramatically with the irradiation time in the presence of TiO_2, TiO_2/Ti_3C_2, TiO_2/Pd and $TiO_2/Pd/Ti_3C_2$. Fig. 4b shows the H_2 evolution rate. All of the TiO_2/Pd, TiO_2/Ti_3C_2 or $TiO_2/Pd/Ti_3C_2$ nanocomposites show superior photocatalytic activity compared to that of pure TiO_2 (0.16 mmol h^{-1} g^{-1}). And as the amount of Pd increases from 1 wt% to 3 wt%, the rate of hydrogen production also increases (Table S1). Similarly, when TiO_2 NSs were combined with single-layer Ti_3C_2, their photocatalytic activity was enhanced; however, this increase was weaker than that of Pd. The rate of decomposition of water to produce hydrogen with $TiO_2/1\%$ Ti_3C_2 was 0.85 mmol h^{-1} g^{-1}, which was 5.3 times that with TiO_2 NSs. As the mass ratio of single-layer Ti_3C_2 increased from 1% to 3%, its photocatalytic activity decreased. This might be due to its larger size, and excessive loading would block the incident light and mask the active reaction sites on the surface of the TiO_2 NSs. It can also be seen that the photocatalytic activity of the composites with both Pd and single-layer Ti_3C_2 was higher than that of the catalysts with only Pd loading or only single-layer Ti_3C_2. In the nanocomposite materials, Ti_3C_2 and Pd worked together to significantly improve the photocatalytic hydrogen production activity of TiO_2 NSs. The $TiO_2/3\%$ Pd/1% Ti_3C_2 heterojunction nanocomposite exhibits the highest hydrogen evolution rate (21.60 mmol h^{-1} g^{-1}), which is 135, 25.4 and 1.5 times higher
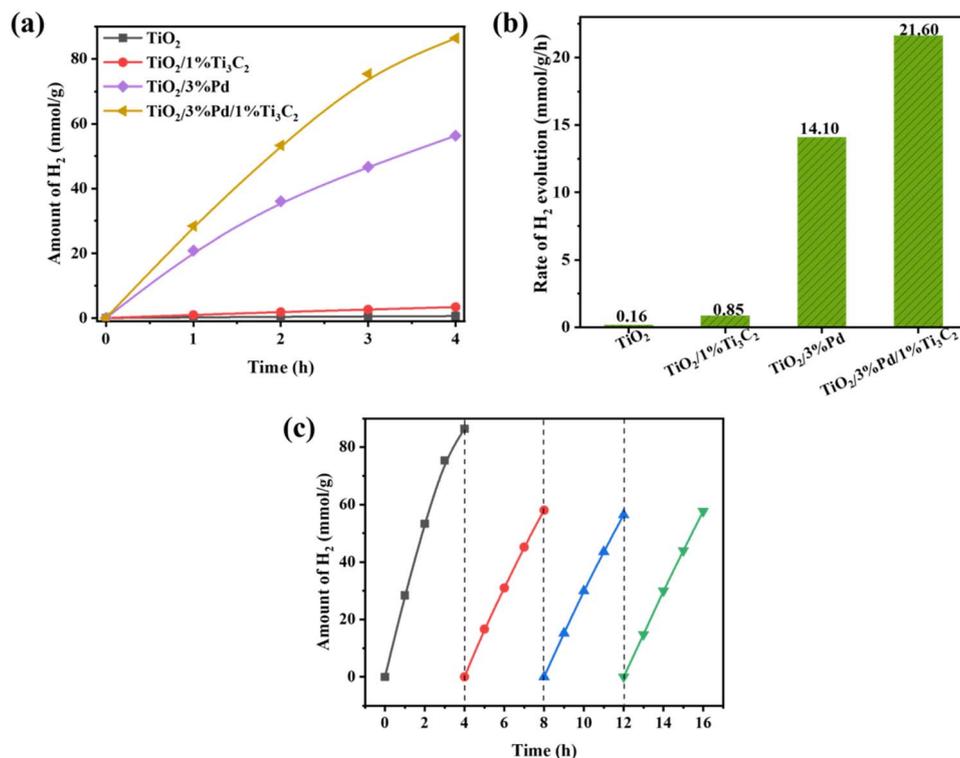
RSC Advances

Paper

Fig. 4 (a) Photocatalytic H$_2$ production activity, (b) H$_2$ production rate and (c) recycling test of TiO$_2$, TiO$_2$/1% Ti$_3$C$_2$, TiO$_2$/3% Pd and TiO$_2$/3% Pd/1% Ti$_3$C$_2$.

than that of the pure TiO$_2$ (0.16 mmol h^{-1} g^{-1}), TiO$_2$/1% Ti$_3$C$_2$ (0.85 mmol h^{-1} g^{-1}) and TiO$_2$/3% Pd (14.10 mmol h^{-1} g^{-1}), respectively. This may be due to the improved separation efficiency of the photogenerated charge carriers in TiO$_2$, as demonstrated by the PL experiment. These results indicate that among the substances that enhance the activity of TiO$_2$ NSs, the role of Pd is the most significant. The amount of single-layer Ti$_3$C$_2$ composite cannot be too high; otherwise, it will have the opposite effect. More importantly, the co-composite and mutual synergy of Pd NPs with monolayer Ti$_3$C$_2$ can significantly improve the H$_2$ production activity of TiO$_2$ NSs. However, during the cyclic experiments conducted under the same conditions as the aforementioned performance tests, the activity for hydrogen (H$_2$) production decreases after four consecutive tests (Fig. 4c). It is speculated that this reduction might be attributed to the loss of the catalyst during the recovery process and the inherent instability of Ti$_3$C$_2$, rendering it susceptible to oxidation.

3.4. Photocatalytic mechanism

Subsequently, *in situ* ESR spectroscopy under simulated sunlight was employed to elucidate the mechanism underlying the enhanced hydrogen production activity by identifying reactive species generated during the photocatalytic reaction. Firstly, TEMPO was chosen to verify the generation of photo-induced electrons by irradiation of the TiO$_2$ hybrid materials. As shown in Fig. 5a, we clearly observed a three-line spectrum with relative intensities of 1 : 1 : 1, and the EPR signal intensity

follows the order: TiO$_2$/3% Pd < TiO$_2$/1% Ti$_3$C$_2$ < TiO$_2$/3% Pd/1% Ti$_3$C$_2$ < TiO$_2$. This trend indicates that TEMPO reacts with photogenerated electrons, and, consequently, the TiO$_2$/3% Pd heterojunction nanocomposite exhibits the strongest electron scavenging capacity. In an aqueous solution, DMPO was employed as a spin-trapping agent to detect hydroxyl radicals (·OH). The DMPO–·OH adduct, formed by the reaction of ·OH with DMPO, was monitored *via* EPR spectroscopy. As shown in Fig. 5b, all Pd- and Ti$_3$C$_2$-loaded TiO$_2$ samples exhibited a characteristic four-line spectrum with relative intensities of 1 : 2 : 2 : 1 upon irradiation. When TiO$_2$/3% Pd hybrid nanostructures were added, the DMPO–·OH signal was the strongest for the different samples, indicating that Pd effectively facilitates the generation of highly oxidative ·OH radicals during photoreaction. Superoxide free radicals (O$_2^{-·}$) are another common intermediate active substance in photocatalytic reactions; they have a longer lifespan and also exhibit excellent practical efficiency. BMPO is a spin trap frequently used for capturing superoxide. The ESR spectra showed that the concentration of O$_2^{-·}$ in the materials with TiO$_2$/3% Pd/1% Ti$_3$C$_2$ hybrid structure is the highest (Fig. 5c). The redox potential of O$_2^{-·}$, being −0.16 eV, indicates that this hybrid structured material has a more negative conduction band position, which can generate more O$_2^{-·}$. In addition, singlet oxygen (^{1}O$_2$) is another important ROS with strong oxidizing activity. TEMP was selected as a spin probe to investigate the formation of ^{1}O$_2$ in the presence of TiO$_2$/Pd/Ti$_3$C$_2$ under light conditions. Compared to TiO$_2$ and TiO$_2$/1% Ti$_3$C$_2$, both TiO$_2$/3% Pd/1% Ti$_3$C$_2$ and TiO$_2$/3% Pd

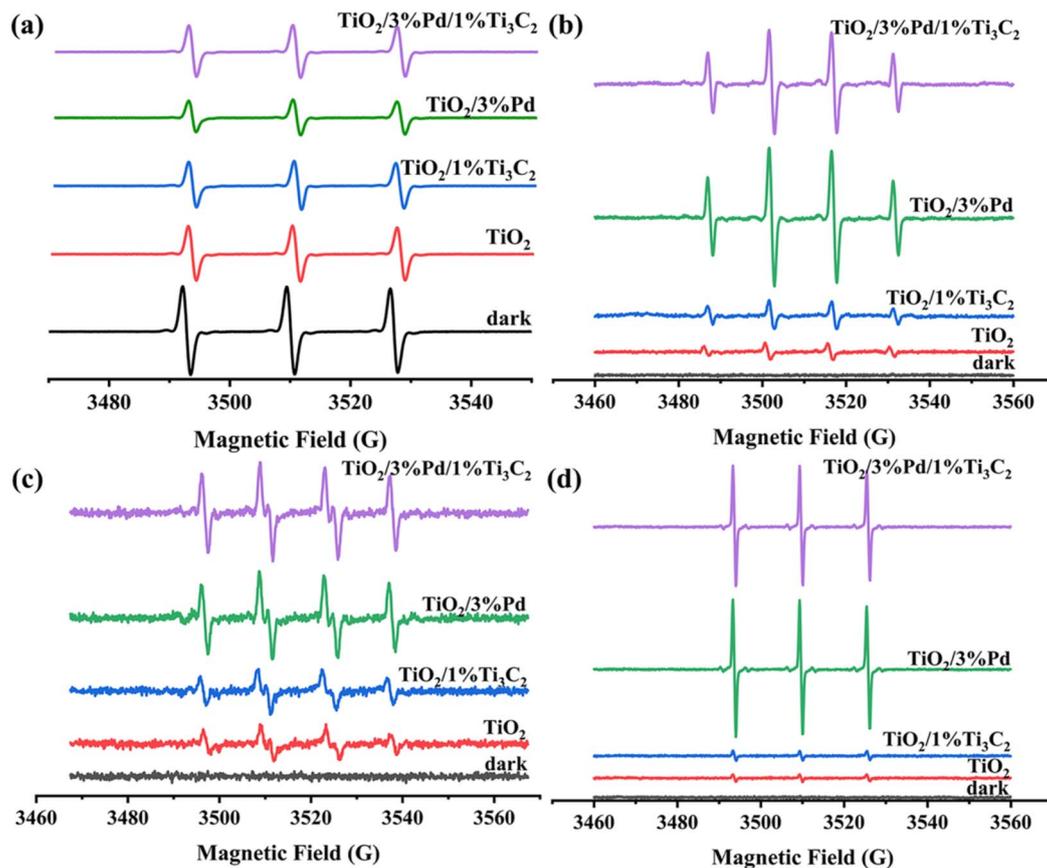**Fig. 5** EPR spectra of (a) TEMPO/e$^-$, (b) DMPO/$\cdot$OH, (c) BMPO/O$_2^{-\cdot}$ and (d) TEMP/^{1}O$_2$ with different catalysts in the dark or with light excitation.

generated very strong ^{1}O$_2$ signals (Fig. 5d), once again demonstrating the positive role of the precious metal Pd in promoting the generation of free radicals during the photocatalysis process. Using ESR spectroscopy, we have demonstrated that photogenerated electrons, $\cdot$OH, O$_2^-$, and ^{1}O$_2$ are formed during photoexcitation of TiO$_2$ and hybrid nanostructured materials, and changes in the levels of free radicals during the photoexcitation reaction were revealed.

On the basis of the physicochemical characterization and photocatalytic analysis, a plausible mechanism pathway for the obtained TiO$_2$/Pd/Ti$_3$C$_2$ heterojunction sample toward H$_2$ generation under light irradiation is explained below and represented in Fig. 6. XPS was used to determine the locations of the valence and conduction bands, and to further elucidate whether a heterojunction exists between them (a structure that supports efficient charge separation). Analysis of the XPS valence band spectra indicated that TiO$_2$ has an $E_{VB,XPS}$ of 2.54 eV (Fig. S3b). The valence band energy of the standard hydrogen electrode can be obtained using the formula:[34] $E_{VB,NHE} = \Phi + E_{VB,XPS} - 4.44$. Here, Φ is the work function of the instrument, with a value of 4.76 eV. According to this formula, the $E_{VB,NHE}$ of TiO$_2$ NSs is calculated to be 2.86 eV. Using formula $E_g = E_{VB,NHE} - E_{CB,NHE}$, the $E_{CB,NHE}$ of TiO$_2$ was calculated to be −0.32 eV. According to previous literature reports, the work function of Pd and Ti$_3$C$_2$ MXene was about 5.3 (ref. 35) and 4.21 eV (ref. 36) vs. the absolute vacuum scale (AVS),

and were calculated to be 0.80 and −0.29 eV (vs. NHE scale), respectively. Under illumination, electrons in the valence band of TiO$_2$ are excited to the conduction band. To investigate the charge transfer process in 2D/0D/2D TiO$_2$/3% Pd/1% Ti$_3$C$_2$ heterojunctions, XPS spectra were recorded; the resulting data are presented in Fig. S4. Generally, shifts in electronic binding energy indicate electron gain or loss. A negative shift corresponds to electron gain, whereas a positive shift indicates electron loss.[37–40] As shown in Fig. S4a and S4b, the XPS spectra reveal a significant increase in the binding energies of Ti 2p and O 1s for the TiO$_2$/3% Pd/1% Ti$_3$C$_2$ heterojunction under light irradiation, indicating electron transfer from the conduction band of TiO$_2$ to Pd or Ti$_3$C$_2$. When TiO$_2$ nanosheets come into contact with Ti$_3$C$_2$ and Pd particles simultaneously, because the work functions of the Ti$_3$C$_2$ monolayer nanosheets and the Pd nanoparticles are lower than the conduction band of TiO$_2$, electrons in the conduction band of TiO$_2$ rapidly transfer from the contact interface to Ti$_3$C$_2$ NSs and accumulate on Pd NPs, while a large number of photogenerated holes remain in the valence band of TiO$_2$ to oxidize methanol (as shown in Fig. 6a). Pd itself acts as an efficient cocatalyst in the composite catalyst, promoting the separation of charge carriers and thus facilitating the generation of oxidizing radicals. Moreover, Pd and Ti$_3$C$_2$ can work synergistically to promote the generation of O$_2^-$. Additionally, since both Ti$_3$C$_2$ and Pd have relatively low Fermi levels, another reaction mechanism may exist when they
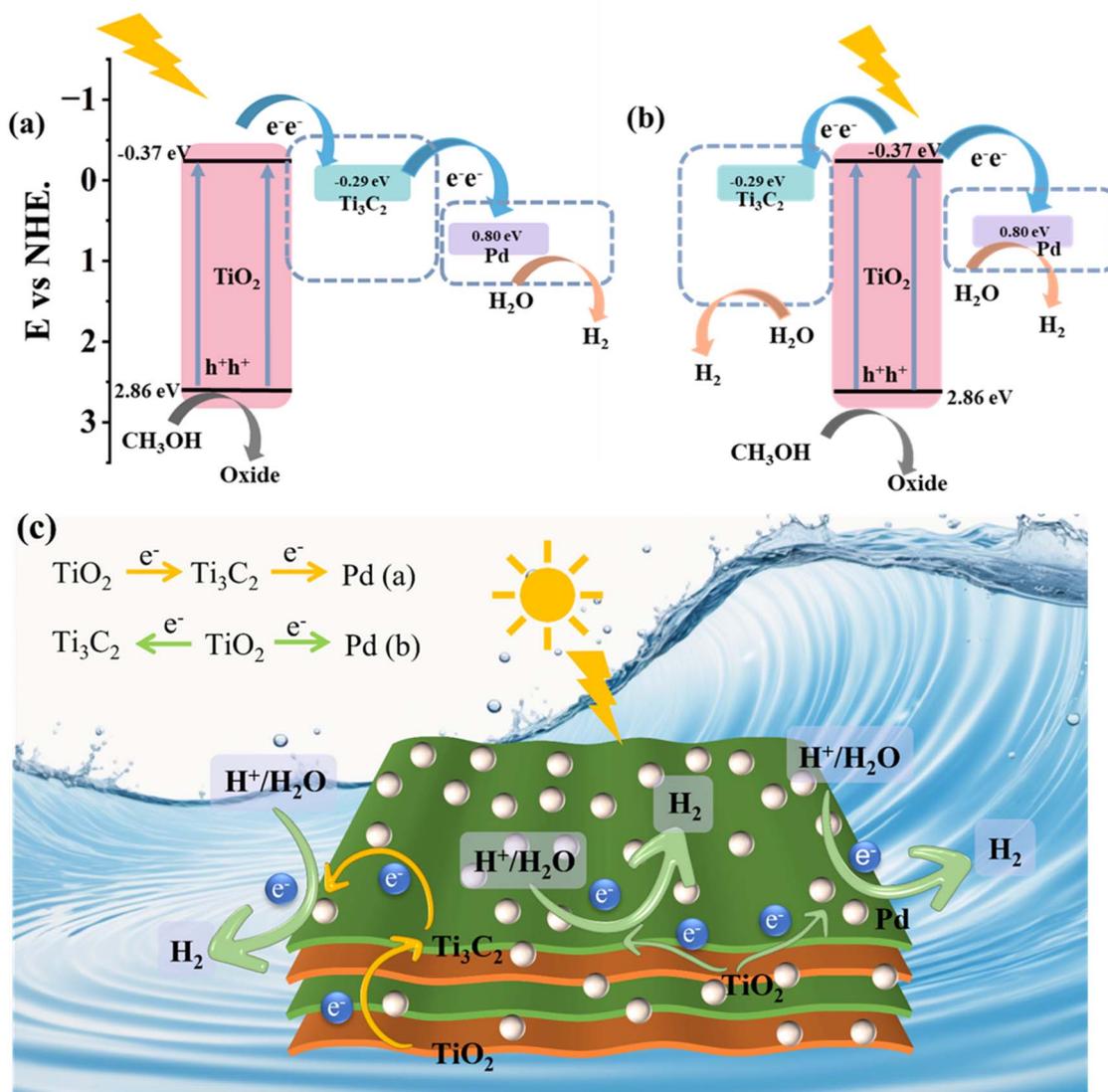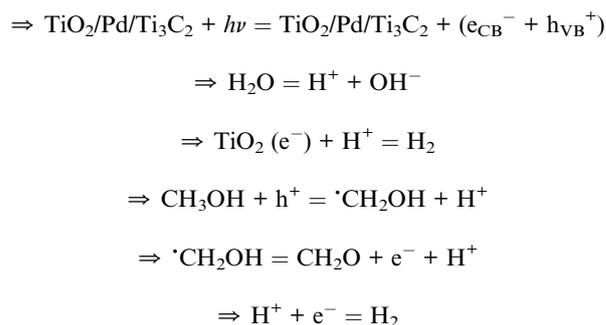
Fig. 6 Band structure alignment of the TiO₂/Pd/Ti₃C₂ heterojunction and the possible photoexcited charge separation and transfer pathways (a and b). Schematic of the photocatalytic mechanism of the TiO₂/3% Pd/1% Ti₃C₂ composite for solar light-assisted H₂ evolution (c).

come into contact at the interface. Photogenerated electrons in the conduction band of TiO₂ will simultaneously transfer to Ti₃C₂ with a slightly lower Fermi level and Pd with an even lower Fermi level, as shown in Fig. 6b. H₂O molecules adsorbed on the surface of the Pd particles and Ti₃C₂ are reduced by photogenerated electrons to form hydrogen. However, the complex transport paths in the composite nanomaterials may affect the ability of the composite material to capture photogenerated electrons, which may be due to the strong electron enrichment ability of Pd and its certain electron transport ability with monolayer Ti₃C₂. In this system, we propose that both reaction mechanisms coexist, and the synergistic interaction between TiO₂ NSs, Pd NPs and Ti₃C₂ NSs in the interface of 2D/0D/2D heterojunction plays a more critical role in enhancing the photocatalytic hydrogen production performance. The entire reaction mechanism pathway for photocatalytic hydrogen generation is described in the following equations:

$$\Rightarrow TiO_2/Pd/Ti_3C_2 + h\nu = TiO_2/Pd/Ti_3C_2 + (e_{CB}^- + h_{VB}^+)$$

$$\Rightarrow H_2O = H^+ + OH^-$$

$$\Rightarrow TiO_2 (e^-) + H^+ = H_2$$

$$\Rightarrow CH_3OH + h^+ = {}^{\cdot}CH_2OH + H^+$$

$$\Rightarrow {}^{\cdot}CH_2OH = CH_2O + e^- + H^+$$

$$\Rightarrow H^+ + e^- = H_2$$

4. Conclusions

In conclusion, we have successfully constructed 2D/0D/2D TiO₂/Pd/Ti₃C₂ heterojunction nanocomposite photocatalysts through the combination of the photoreduction method and

electrostatic self-assembly technology, which can significantly enhance the hydrogen production efficiency. The research results show that after introducing a small amount of single-layer Ti_3C_2 and Pd NPs, the photocatalytic H_2 production performance of TiO_2 is significantly enhanced by 135 times. When the mass fractions of monolayer Ti_3C_2 and Pd NPs are 1% and 3% respectively, the TiO_2/Pd/Ti_3C_2 nanocomposite catalyst exhibits the optimal photocatalytic activity, with a H_2 production rate reaching 21.6 mmol h^{-1} g^{-1}. The improvement of photocatalytic performance is mainly attributed to Pd as an excellent auxiliary catalyst, which not only promotes the transfer of photogenerated electrons but also enhances the separation efficiency of charge carriers, thereby facilitating the generation of oxidative free radicals. Moreover, there is a synergistic effect between Ti_3C_2 and Pd, which further promotes the formation of $O_2^{-\cdot}$ free radicals. This study provides new ideas and a theoretical basis for the design of efficient multi-interface interaction photocatalysts and for the analysis of reaction mechanisms.

Conflicts of interest

There are no conflicts to declare.

Data availability

Data will be available upon request.

Supplementary information: AFM image of Ti_3C_2, XPS survey spectra of TiO_2/3%Pd/1%Ti_3C_2, the band gap and the valence band position of TiO_2 NSs, XPS high-resolution spectra of Ti 2p and O 1s, the H_2 production rates of other composite materials. See DOI: https://doi.org/10.1039/d5ra06368j.

Acknowledgements

References

1 C. W. Hamilton, R. T. Baker, A. Staubitz and I. Manners, B–N compounds for chemical hydrogen storage, *Chem. Soc. Rev.*, 2009, **38**, 279–293.

2 M. Ma, Y. Fang, Z. Huang, S. Wu, W. He, S. Ge, Z. Zheng, Y. Zhou, W. Fa and X. Wang, Mechanistic Insights Into H_2O Dissociation in Overall Photo-/Electro-Catalytic CO_2 Reduction, *Angew. Chem., Int. Ed.*, 2025, e202425195.

3 Y. Dong, Q. Han, Q. Hu, C. Xu, C. Dong, Y. Peng, Y. Ding and Y. Lan, Carbon quantum dots enriching molecular nickel polyoxometalate over CdS semiconductor for photocatalytic water splitting, *Appl. Catal., B*, 2021, **293**, 120214.

4 Y. Zhao, Y. Zhao, R. Shi, B. Wang, G. I. N. Waterhouse, L. Z. Wu, C. H. Tung and T. Zhang, Tuning oxygen vacancies in ultrathin TiO_2 nanosheets to boost photocatalytic nitrogen fixation up to 700 nm, *Adv. Mater.*, 2019, **31**, 1806482.

5 D. Kujawa, A. Grzegórska, A. Zielinska-Jurek, M. Fandzloch, O. Bezkrovnyi and P. Głuchowski, Enhancement of carbamazepine photodegradation using hybrid of phosphorescent carbon dots coupled with highly porous TiO_2 photocatalyst, *Dalton Trans.*, 2025, **54**, 1504–1520.

6 Y. Wu, X. Chen, J. Cao, Y. Zhu, W. Yuan, Z. Hu, Z. Ao, G. W. Brudvig, F. Tian, J. C. Yu and C. Li, Photocatalytically recovering hydrogen energy from wastewater treatment using MoS_2@TiO_2 with sulfur/oxygen dual-defect, *Appl. Catal., B*, 2022, **303**, 120878.

7 K. Ma, Y. Dong, M. Zhang, C. Xu and Y. Ding, A homogeneous Cu-based polyoxometalate coupled with mesoporous TiO_2 for efficient photocatalytic H_2 production, *J. Colloid Interface Sci.*, 2021, **587**, 613–621.

8 S. Pany, B. Naik, S. Martha and K. Parida, Plasmon induced nano Au particle decorated over S, N-modified TiO_2 for exceptional photocatalytic hydrogen evolution under visible light, *ACS Appl. Mater. Interfaces*, 2014, **6**, 839–846.

9 L. Ji, Y. Zhang, S. Miao, M. Gong and X. Liu, In situ synthesis of carbon doped TiO_2 nanotubes with an enhanced photocatalytic performance under UV and visible light, *Carbon*, 2017, **125**, 544–550.

10 J. Ryu, S. H. Lee, D. H. Nam and C. B. Park, Rational design and engineering of quantum-dot-sensitized TiO_2 nanotube arrays for artificial photosynthesis, *Adv. Mater.*, 2011, **23**, 1883–1888.

11 W. W. He, J. Cai, X. Jiang, J.-J. Yin and Q. B. Meng, Generation of reactive oxygen species and charge carriers in plasmonic photocatalytic Au@TiO_2 nanostructures with enhanced activity, *Phys. Chem. Chem. Phys.*, 2018, **20**, 16117–16125.

12 W. W. Tie, S. S. Bhattacharyya, T. Ma, S. Yuan, M. Chen, W. W. He and S. H. Lee, Improving photoexcited carrier separation through Z-scheme $W_{18}O_{49}$/BiOBr heterostructure coupling carbon quantum dots for efficient photoelectric response and tetracycline photodegradation, *Carbon*, 2025, **231**, 119707.

13 X. Meng, L. Liu, S. Ouyang, H. Xu, D. Wang, N. Zhao and J. Ye, Nanometals for solar-to-chemical energy conversion: from semiconductor-based photocatalysis to plasmon-mediated photocatalysis and photo-thermocatalysis, *Adv. Mater.*, 2016, **28**, 6781–6803.

14 C. Li, Y. Wang, Y. Chen, H. Jia and W. He, Synergistic photocatalytic nanozymes to promote contaminant removal and hydrogen production, *Mater. Today Sustain.*, 2023, **24**, 100537.

15 M. Naguib, O. Mashtalir, J. Carle, V. Presser, J. Lu, L. Hultman, Y. Gogotsi and M. W. Barsoum, Two-dimensional transition metal carbides, *ACS Nano*, 2012, **6**, 1322–1331.

16 H. J. Guan, T. D. Guo, S. H. Liu, D. Pan, H. M. Jia and W. W. He, AuCo Nanoparticles Inserted between the Layers of Ti_3C_2: An Efficient Nanozyme for Aliphatic Nitro-to-Amine Reduction, *ChemNanoMat*, 2025, 2500171.

17 B. Wang, M. Wang, F. Liu, Q. Zhang, S. Yao, X. Liu and F. Huang, Ti_3C_2: An ideal co-catalyst?, *Angew Chem. Int. Edit.*, 2020, **59**, 1914–1918.

18 H. Q. Geng, Z. J. Li, Q. Liu, Q. Yang, H. M. Jia, Q. Chen, A. G. Zhou and W. W. He, Boosting the peroxidase-like activity of Pt nanozymes by a synergistic effect of Ti_3C_2 nanosheets for dual mechanism detection, *Dalton Trans.*, 2022, **51**, 11693–11702.

19 Y. Zhao, G. Zuo, Y. Wang, W. L. Teo, A. Xie, Y. Guo, Y. Dai, W. Zhou, D. Jana and Q. Xian, Ultrathin $ZnIn_2S_4$ nanosheets anchored on Ti_3C_2TX MXene for photocatalytic H_2 evolution, *Angew. Chem. Int. Ed.*, 2020, **132**, 11383–11388.

20 Y. Yang, J. L. Kuang and W. B. Cao, In situ hydrothermal synthesis of schottky compound Ti_2CT_x/TiO_2 for efficient photocatalytic oxidation NO_x removal, *J. Phys. Chem. C*, 2025, **129**, 1702–1713.

21 J. Li, L. Zhao, S. Wang, J. Li, G. Wang and J. Wang, In situ fabrication of 2D/3D g-C_3N_4/Ti_3C_2 (MXene) heterojunction for efficient visible-light photocatalytic hydrogen evolution, *Appl. Surf. Sci.*, 2020, **515**, 145922.

22 B. Sun, P. Qiu, Z. Liang, Y. Xue, X. Zhang, L. Yang, H. Cui and J. Tian, The fabrication of 1D/2D CdS nanorod@Ti_3C_2 MXene composites for good photocatalytic activity of hydrogen generation and ammonia synthesis, *Chem. Eng. J.*, 2021, **406**, 127177.

23 E. Hussain, A. Tanveer, M. Z. Abid, M. Z. Waleed and K. Rafiq, Scaling up the catalytic hydrogen generation on a Rh−Cu@$Ti_3C_2T_x$−CN system: A strategic approach for green fuel production, *ACS Appl. Energy Mater.*, 2025, **8**, 4428–4440.

24 H. Q. Geng, Y. P. Ren, G. Qin, T. Wen, Q. Liu, H. Y. Xu and W. W. He, Ti_3C_2 nanosheets with broad-spectrum antioxidant activity for cytoprotection against oxidative stress, *RSC Adv.*, 2022, **12**, 11128–11138.

25 M. Tahir, Investigating the influential effect of etchant time in constructing 2D/2D HCN/MXene heterojunction with controlled growth of TiO_2 NPs for stimulating photocatalytic H_2 production, *Energy Fuels*, 2021, **35**, 6807–6822.

26 B. Li, H. H. Zhu, H. Zhang, L. N. Xiao and S. Y. He, Janus Flower-Like Hollow TiO_2 Photocatalysts Bearing RuO_2 and Pt Nanoparticles for Solar-Light-Driven Catalytic H_2 Evolution, *ACS Appl. Nano Mater.*, 2023, **6**, 18978–18987.

27 L. Biswal, L. Acharya, B. P. Mishra, S. Das, G. Swain and K. Parida, Interfacial Solid-State Mediator-Based Z-Scheme Heterojunction TiO_2@Ti_3C_2/$MgIn_2S_4$ microflower for efficient photocatalytic pharmaceutical micropollutant degradation and hydrogen generation: stability, kinetics, and mechanistic insights, *ACS Appl. Energy Mater.*, 2023, **6**, 2081–2096.

28 J. X. Yang, W. B. Yu and C. F. Li, PtO nanodots promoting Ti_3C_2 MXene in-situ converted Ti_3C_2/TiO_2 composites for photocatalytic hydrogen production, *Chem. Eng. J.*, 2021, **420**, 129695.

29 T. Su, Z. D. Hood and M. Naguib, Monolayer $Ti_3C_2T_x$ as an effective co-catalyst for enhanced photocatalytic hydrogen production over TiO_2, *ACS Appl. Energy Mater.*, 2019, **2**, 4640–4651.

30 Y. Y. Mao, F. M. Jia, T. Y. Jing, T. T. Li, H. M. Jia and W. W. He, Enhanced multiple enzymelike activity of PtPdCu trimetallic nanostructures for detection of Fe^{2+} and evaluation of antioxidant capability, *ACS Sustainable Chem. Eng.*, 2021, **9**, 569–579.

31 H. M. Zhu, B. F. Yang, J. Xu, Z. P. Fu, M. W. Wen, T. Guo, S. Q. Fu, J. Zuo and S. Y. Zhang, Construction of Z-scheme type CdSAu-TiO_2 hollow nanorod arrays with enhanced photocatalytic activity, *Appl. Catal., B*, 2009, **90**, 463–469.

32 M. C. Liu, P. Ye, M. Wang, L. L. Wang, C. Wu, J. Xu and Y. P. Chen, 2D/2D Bi-MOF-Derived $BiOCl/MoS_2$ nanosheets S-scheme heterojunction for effective photocatalytic degradation, *J. Environ. Chem. Eng.*, 2022, **10**, 108436.

33 H. M. Jia, B. B. Zhang, W. W. He, Y. Xiang and Z. Zheng, Mechanistic insights into the photoinduced charge carrier dynamics of BiOBr/CdS nanosheet heterojunctions for photovoltaic application, *Nanoscale*, 2017, **9**, 3180–3187.

34 Y. X. Liu, R. X. Li, P. C. Gao, Y. Zhang, H. M. Ma, J. J. Yang, B. Du and Q. Wei, A signal-off sandwich photoelectrochemical immunosensor using TiO_2 coupled with CdS as the photoactive matrix and copper(II) ion as inhibitor, *Biosens. Bioelectron.*, 2015, **65**, 97–102.

35 M. Todorova, K. Reuter and M. Scheffler, Oxygen overlayers on Pd (111) studied by density functional theory, *J. Phys. Chem. B*, 2004, **108**, 14477–14483.

36 K. L. Huang, C. Y. Lv, C. H. Li, H. C. Bai and X. C. Meng, Ti_3C_2 MXene supporting platinum nanoparticles as rapid electrons transfer channel and active sites for boosted photocatalytic watersplitting over g-C_3N_4, *J. Colloid Interface Sci.*, 2023, **636**, 21–32.

37 Q. Zhou, K. J. Zhang, Y. R. Su, X. H. Wu, T. Y. Gao and G. H. Wang, 2D/1D $CaIn_2S_4/TiO_2$ S-Scheme Heterojunction: In-Situ Hydrothermal Synthesis and Enhanced Photocatalytic H_2 Evolution, *J. Materiomics*, 2025, **11**, 100987.

38 T. Y. Gao, X. F. Liu, K. Wang, J. Wang, X. H. Wu and G. H. Wang, Sponge-like Inorganic–Organic S-Scheme Heterojunction for Efficient Photocatalytic Hydrogen Evolution, *J. Colloid Interface Sci.*, 2025, **692**, 137475.

39 T. Y. Gao, X. F. Liu, Q. S. Feng, X. H. Wu, J. Wang and G. H. Wang, Microwave assisted rapid synthesis of TiO_2 NFs@COF S-scheme heterojunction photocatalyst for highly efficient photocatalytic hydrogen evolution, *J. Colloid Interface Sci.*, 2025, **698**, 138075.

40 T. Y. Gao, D. Shi, X. F. Liu, X. H. Wu and G. H. Wang, Investigating the charge transfer mechanism of 1D/2D $ZnO/SnIn_4S_8$ S-scheme heterojunction for efficient photocatalytic hydrogen evolution, *J. Mater. Sci. Technol.*, 2026, **251**, 241–251.